A Fully Nonlinear Boussinesq Model in Generalized Curvilinear Coordinates

by

Fengyan Shi, Robert A. Dalrymple, James T. Kirby,
Qin Chen and Andrew Kennedy

RESEARCH REPORT NO. CACR-99-06
November 1999

CENTER FOR APPLIED COASTAL RESEARCH

Ocean Engineering Laboratory
University of Delaware
Newark, Delaware 19716

A Fully Nonlinear Boussinesq Model in Generalized Curvilinear Coordinates

by

FENGYAN SHI, ROBERT A. DALRYMPLE, JAMES T. KIRBY,
QIN CHEN AND ANDREW KENNEDY

RESEARCH REPORT NO. CACR-99-06
NOVEMBER 1999

CENTER FOR APPLIED COASTAL RESEARCH
OCEAN ENGINEERING LABORATORY
UNIVERSITY OF DELAWARE
NEWARK, DE 19716

REPORT DOCUMENTATION PAGE

Form Approved
OMB NO. 0704-0188

1. AGENCY USE ONLY (Leave Blank)	2. REPORT DATE November 1999	3. REPORT TYPE AND DATES COVERED Technical Report

4. TITLE AND SUBTITLE A Fully Nonlinear Boussinesq Model in Generalized Curvilinear Coordinates	5. FUNDING NUMBERS DAAG55-98-1-0173
6. AUTHOR(S) Fengyan Shi, Robert A. Dalrymple, James T. Kirby, Qin Chen and Andrew Kennedy	

7. PERFORMING ORGANIZATION NAME(S) AND ADDRESS(ES) Center for Applied Coastal Research University of Delaware Newark, DE 19716	8. PERFORMING ORGANIZATION REPORT NUMBER CACR-99-06

9. SPONSORING / MONITORING AGENCY NAME(S) AND ADDRESS(ES) U. S. Army Research Office P.O. Box 12211 Research Triangle Park, NC 27709-2211	10. SPONSORING / MONITORING AGENCY REPORT NUMBER ARO 37548.2-EV

11. SUPPLEMENTARY NOTES
    The views, opinions and/or findings contained in this report are those of the author(s) and should not be construed as an official Department of the Army position, policy or decision, unless so designated by other documentation.

12 a. DISTRIBUTION / AVAILABILITY STATEMENT Approved for public release; distribution unlimited.	12 b. DISTRIBUTION CODE

13. ABSTRACT (Maximum 200 words)

Based on the fully nonlinear Boussinesq equations in Cartesian coordinates, the equations in generalized coordinates are derived adapt computations to irregularly-shaped shorelines, such as harbors, bays and tidal inlets, and to make computations more efficient in large nearshore regions. Contravariant components of velocity vectors are employed in the derivation instead of the normal comonents in curvilinear coordinates or original components in Cartesian coordinates, which greatly simplifies the equations in generatlized curvilinear coordinates. A high-order finite difference scheme with staggered grids in the image domain is adopted in the numerical model. The model is applied to five examples involving irregular coordinate systems. The results of these cases are in good agreement with analytical results, experimental data, and the results from the uniform grid model, which shows that the model has good accuracy and efficiency in dealing with th computations of nonlinear surface geravity waves in domains complicated geometries.

14. SUBJECT TERMS Coastal engineering, wave model, Boussinesq model, tidal inlets			15. NUMBER OF PAGES 45
			16. PRICE CODE

17. SECURITY CLASSIFICATION OR REPORT UNCLASSIFIED	18. SECURITY CLASSIFICATION ON THIS PAGE UNCLASSIFIED	19. SECURITY CLASSIFICATION OF ABSTRACT UNCLASSIFIED	20. LIMITATION OF ABSTRACT UL

NSN 7540-01-280-5500

Standard Form 298 (Rev.2-89)
Prescribed by ANSI Std. 239-18
298-102

A fully nonlinear Boussinesq model
in generalized curvilinear coordinates

Fengyan Shi, Robert A. Dalrymple, James T. Kirby,

Qin Chen and Andrew Kennedy

Center for Applied Coastal Research,
University of Delaware, Newark, DE 19716, USA

Fax: (302) 831 1228, email: fyshi@coastal.udel.edu

Abstract

Based on the fully nonlinear Boussinesq equations in Cartesian coordinates, the equations in generalized coordinates are derived to adapt computations to irregularly-shaped shorelines, such as harbors, bays and tidal inlets, and to make computations more efficient in large nearshore regions. Contravariant components of velocity vectors are employed in the derivation instead of the normal components in curvilinear coordinates or original components in Cartesian coordinates, which greatly simplifies the equations in generalized curvilinear coordinates. A high-order finite difference scheme with staggered grids in the image domain is adopted in the numerical model. The model is applied to five examples involving irregular coordinate systems. The results of these cases are in good agreement with analytical results, experimental data, and the results from the uniform grid model, which shows that the model has good accuracy and efficiency in dealing with the computations of nonlinear surface gravity waves in domains with complicated geometries.

1

1 Introduction

Boussinesq models for surface gravity waves have been proved to be effective tools to simulate wave propagation in coastal regions. Since the introduction of the standard Boussinesq equations for variable water depth by Peregrine (1967), numerical models based on his equations have been developed by many researchers (Goring 1978; Abbott *et al.* 1979, 1984; Elgar & Guza 1985; Liu, Yoon & Kirby 1985; Rygg 1988) and have been shown to give good predictions in comparison with field data or laboratory data, when applied within their range of validity. Recently, extended forms of Boussinesq equations were derived by Madsen, Murray & Sørensen (1991) and Nwogu (1993), among others, to improve dispersion relationships in intermediate water depths and to simulate wave propagation from relatively deep to shallow water. Wei & Kirby (1995) developed a high-order numerical model based on Nwogu's equations and provided additional validation tests of the model. More recently, fully nonlinear Boussinesq equations were derived by Wei *et al.* (1995). The resulting equations not only have improved linear dispersion properties in intermediate water depths but they are not limited to small amplitude waves. A time-domain numerical model based on the equations was then developed and verified against a broad range of experimental data (see Wei and Kirby, 1998; Kennedy *et al.*, 1999 and Chen *et al.*, 1999a). Chen *et al.* (1999b) applied the fully nonlinear Boussinesq model with the incorporation of energy dissipation by wave breaking to investigate the fully-coupled interaction of surface waves with rip currents and the nearshore circulation generated by wave breaking on a barred beach with a rip channel.

Most of the numerical Boussinesq models are solved by the finite difference method using rectangular grids. However, the geometric complexity of the general coastal environment together with the rapid change in wavelength as waves move from deep to

2

shallow water makes the use of undistorted grids in the models somewhat problematic. Typically, a model grid chosen to study the entire range from deep water to the shoreline results in problems such that waves are over-resolved in deep water and under-resolved in shallow water. To resolve a broad spectrum of wind waves, the time-domain Boussinesq model with a regular grid spacing may become too expensive to be used in large nearshore regions. Moreover, complicated geometries, such as harbors and tidal inlets, make the computation very expensive because of local resolution problems, and in addition, the stair-stepping boundaries associated with rectangular grids may decrease the computational accuracy. To deal with such problems, irregular grid methods are generally used through coordinate transformations, such that the physical irregularly shaped domain is transformed into a regular image domain where the finite difference computations are carried out.

There are numerous examples of irregular grid methods in the study of waves. Numerical models based on the parabolic approximation of the mild-slope equation for linear wave propagation in a non-orthogonal coordinate system were developed by Tsay and Liu (1982), Isobe (1986), Liu and Boissevain (1988), Kaku and Kirby (1988), Kirby (1988), Kirby et al. (1994). Dalrymple et al. (1994) used spectral methods to study forward-propagating water waves in conformally-mapped channels. An example of the use of a curvilinear grid system to solve Boussinesq-type equations is given in Wang et al. (1992), who studied solitary wave scattering by a vertical cylinder.

Irregular grid methods are also widely used in numerical modeling of large-scale oceanographic problems involving shallow water equations. Non-orthogonal boundary-fitted grid models were developed (e.g., Sheng 1986; Chen, Zheng and Zhu, 1999) for modeling coastal and estuarine processes. Shi and Sun (1995) developed a self-

3

adaptive grid model for computing the time dependent moving boundary problem of storm surge flooding using the shallow water equations.

Generally, there are three coordinate transformation methods for the transformation of hyperbolic-type equations (including Boussinesq-type equations if only considering leading order terms). The first method is to transform the independent variables only, retaining the unchanged primitive variable (u, v, η) (see, for example, Häuser *et al.*, 1985, 1986; Raghunath *et al.* 1987; Borthwick and Barber, 1992). In this method, the transformed expressions of both equations and boundary conditions are more complex than their Cartesian counterparts. It is not efficient to use the method to treat the fully nonlinear Boussinesq equations since the higher order differential terms in the equations would make the expressions very complicated. A typical example is that u_{xx} may be extended into six terms in the curvilinear coordinate and there are even more terms for higher order differentials. The second method is the adoption of the tangential velocity in curvilinear coordinates (e.g., Chen, Zheng and Zhu, 1999) or the covariant component of the velocity vector (Warsi, 1998) in the coordinate transformation. The resulting equations from these methods are relatively simple compared with the equations from the former method. However, difficulties were found in realizing lateral slip boundary conditions in non-orthogonal curvilinear coordinates. The third method is the contravariant component method (Warsi, 1998). The contravariant components of the velocity vector can be regarded as generalized components of velocity in the transformed image domain. Several advantages of using the contravariant velocity have been recognized in the derivations of hyperbolic-type equations, as shown by Sheng (1986), among others. Shi and Sun (1995,1997) introduced the contravariant components in their coordinate transformation of shallow water equations and easily obtained the kinematical lateral boundary conditions,

4

i.e., the contravariant components of velocity are zero at boundaries. Furthermore Shi and Sun (1998) derived a new set of equations for the shallow water equations in terms of contravariant velocity and surface elevation in order to solve the transformed equations by using an alternating-direction-implicit scheme.

In this paper, contravariant velocity techniques are used in the coordinate transformation. Fully nonlinear Boussinesq equations in terms of contravariant components of velocity vector at a reference elevation z_α and the surface elevation are derived in generalized curvilinear coordinates based on the fully nonlinear Boussinesq equations in Cartesian coordinates. Following the work of Wei and Kirby (1995) and Wei *et al.* (1995), a fourth-order Adams-Bashforth-Moulton predictor-corrector scheme is employed in the numerical model to perform the time integration. Unlike the spatial discretization in Wei *et al.* (1995), we use a staggered grid system in the transformed image domain. The first-order spatial derivative terms are discretized to fourth-order accuracy by using standard five-point finite-differencing, and the dispersive terms are discretized to second-order accuracy. This ensures that the truncation error does not contain terms which are mathematically similar to the actual dispersive terms.

The numerical model is then applied to five cases involving irregular coordinate systems. The first is wave evolution in a rectangular basin with a computational curvilinear grid. Consistency is found between the curvilinear grid model and a uniform rectangular grid model. The second case is wave shoaling on a sloping beach. Here, the element Courant number at every grid point is kept the same everywhere through adjustments of the grid size. The example illustrates the gains in efficiency afforded by the method in an open coastal application. The third case is wave propagation in a circular channel in which a curvilinear grid is generated. The fourth case examines diffraction of a solitary wave by a straight vertical wall at normal incidence. Locally

5

fine grids are generated in this case around the tip of the wall to resolve the scale of the wall. This case shows that the present model is capable of the computation of the nonlinear wave propagation with good accuracy. Finally, the model is applied to Ponce de Leon Inlet (Florida, USA). Boundary-fitted grids with high resolution near structures and inside the inlet are generated and monochromatic waves are simulated.

2   Equations in Generalized curvilinear coordinates

The fully nonlinear Boussinesq equations in Cartesian coordinates (Wei *et al.*, 1995) are written in terms of a reference velocity $\mathbf{u} = (u, v)$ at a reference elevation z_α. The mass conservation equation can be written as

$$\eta_t + \nabla \cdot \mathbf{M} = 0, \tag{1}$$

where $\mathbf{M}$ is the depth-integrated volume flux given by

$$\begin{aligned}
\mathbf{M} &= (h+\eta)\mathbf{u} + (h+\eta)[\frac{z_\alpha^2}{2} - \frac{1}{6}(h^2 - h\eta + \eta^2)]\nabla(\nabla \cdot \mathbf{u}) \\
&\quad + (h+\eta)[z_\alpha + \frac{1}{2}(h-\eta)]\nabla[\nabla \cdot (h\mathbf{u})],
\end{aligned} \tag{2}$$

in which η is the free surface elevation relative to the still water level and h is the still water depth. The associated momentum conservation equation is

$$\mathbf{u}_t + (\mathbf{u} \cdot \nabla)\mathbf{u} + g\nabla\eta + \mathbf{V_1} + \mathbf{V_2} = 0, \tag{3}$$

where g is the gravitational acceleration and $\mathbf{V_1}$ and $\mathbf{V_2}$ are the dispersive Boussinesq terms:

$$\mathbf{V_1} = \frac{z_\alpha^2}{2}\nabla(\nabla \cdot \mathbf{u}_t) + z_\alpha\nabla[\nabla \cdot (h\mathbf{u}_t)] - \nabla[\frac{1}{2}\eta^2\nabla \cdot \mathbf{u}_t + \eta\nabla \cdot (h\mathbf{u}_t)], \tag{4}$$

$$\begin{aligned}
\mathbf{V_2} &= \nabla\{(z_\alpha - \eta)(\mathbf{u} \cdot \nabla)[\nabla \cdot (h\mathbf{u})] + \frac{1}{2}(z_\alpha^2 - \eta^2)(\mathbf{u} \cdot \nabla)(\nabla \cdot \mathbf{u})\} \\
&\quad + \frac{1}{2}\nabla\{[\nabla \cdot (h\mathbf{u}) + \eta\nabla \cdot \mathbf{u}]^2\}.
\end{aligned} \tag{5}$$

6

A coordinate transformation is introduced in the general form

$$\xi_1 = \xi_1(x, y), \quad \xi_2 = \xi_2(x, y), \tag{6}$$

where (ξ_1, ξ_2) are new independent variables in the transformed image domain. Referring to Figure 1, boundaries $\Gamma_1, \Gamma_2, \Gamma_3$ and Γ_4 in the physical domain (x, y) become Π_1, Π_2, Π_3 and Π_4 respectively in the image domain (ξ_1, ξ_2).

Instead of (u, v) in Cartesian coordinates, the contravariant components of the velocity vector at z_α are introduced as the dependent variables in the curvilinear coordinate. In the tensor space, a velocity vector can be expressed as two components of any covariant basis, i.e.

$$\mathbf{u} = u^i \mathbf{g}_i, \tag{7}$$

where u^i are the contravariant components of the covariant basis $\mathbf{g}_i$. As a simple example, (u, v) may be the contravariant components of the covariant basis $(\mathbf{i}, \mathbf{j})$ in Cartesian coordinates. In the present curvilinear coordinates, $u^i = (U, V)$, in which (U, V) are the contravariant components of the covariant basis $(\mathbf{g}_1, \mathbf{g}_2)$. According to the relationships among components in different basis:

$$u^k = \frac{\partial x^k}{\partial x^{i'}} u^{i'}, \tag{8}$$

where $()'$ denotes the new basis. (U, V) can be described by (u, v) in Cartesian coordinates as:

$$U = \frac{1}{\sqrt{g_0}}(u y_{\xi_2} - v x_{\xi_2}), \tag{9}$$

$$V = \frac{1}{\sqrt{g_0}}(-u y_{\xi_1} + v x_{\xi_1}), \tag{10}$$

where g_0 is the determinant of the metric tensor defined by

$$g_0 = \begin{vmatrix} g_{11} & g_{12} \\ g_{21} & g_{22} \end{vmatrix}, \tag{11}$$

7

and where g_{ij} is the covariant metric:

$$g_{ij} = \frac{\partial x^{i'}}{\partial x^i}\frac{\partial x^{i'}}{\partial x^j}. \tag{12}$$

Using the relations:

$$\frac{\partial y}{\partial \xi_2} = \sqrt{g_0}\frac{\partial \xi_1}{\partial x}, \quad \frac{\partial x}{\partial \xi_2} = -\sqrt{g_0}\frac{\partial \xi_1}{\partial y}$$
$$\frac{\partial y}{\partial \xi_1} = -\sqrt{g_0}\frac{\partial \xi_2}{\partial x}, \quad \frac{\partial x}{\partial \xi_1} = \sqrt{g_0}\frac{\partial \xi_2}{\partial y} \tag{13}$$

yields the definition of (U, V):

$$U = u\frac{\partial \xi_1}{\partial x} + v\frac{\partial \xi_1}{\partial y} = \frac{d\xi_1}{dt}, \tag{14}$$

$$V = u\frac{\partial \xi_2}{\partial x} + v\frac{\partial \xi_2}{\partial y} = \frac{d\xi_2}{dt}. \tag{15}$$

Equations (14) and (15) indicate that (U, V) can be regarded as generalized velocities in the generalized coordinates.

From (9) and (10), we can also get the relationship between (U, V) and the velocity components (u_n, v_n) normal to the curvilinear coordinates (Shi and Zheng, 1996):

$$u_n = \frac{\sqrt{g_0}}{\sqrt{g_{22}}}U, \tag{16}$$

$$v_n = \frac{\sqrt{g_0}}{\sqrt{g_{11}}}V. \tag{17}$$

Equations (16) and (17) show that (U, V) are stretched velocity components normal to the curvilinear coordinates. The introduction of (U, V) makes it convenient to obtain the lateral boundary conditions as shown in Section 4.

Equation(1) and (2) are now written in tensor-invariant forms:

$$\eta_t + \frac{1}{\sqrt{g_0}}\frac{\partial}{\partial x^k}(\sqrt{g_0}M^k) = 0, \tag{18}$$

8

$$M^k = (h+\eta)u^k + (h+\eta)[\frac{z_\alpha^2}{2} - \frac{1}{6}(h^2 - h\eta + \eta^2)][\frac{1}{\sqrt{g_0}}\frac{\partial}{\partial x^l}(\sqrt{g_0}u^l)]!^k$$

$$+(h+\eta)[z_\alpha + \frac{1}{2}(h-\eta)][\frac{1}{\sqrt{g_0}}\frac{\partial}{\partial x^l}(\sqrt{g_0}hu^l)]!^k. \tag{19}$$

The tensor-invariant forms of the momentum equations (3), (4) and (5) are:

$$\frac{\partial u^k}{\partial t} + g\eta!^k + u^l u_{,l}^k + V_1^k + V_2^k = 0, \tag{20}$$

$$V_1^k = \frac{z_\alpha^2}{2}[\frac{1}{\sqrt{g_0}}\frac{\partial}{\partial x^l}(\sqrt{g_0}u_t^l)]!^k$$

$$+z_\alpha[\frac{1}{\sqrt{g_0}}\frac{\partial}{\partial x^l}(\sqrt{g_0}hu_t^l)]!^k$$

$$-[\frac{\eta^2}{2\sqrt{g_0}}\frac{\partial}{\partial x^l}(\sqrt{g_0}u_t^l) + \frac{\eta}{\sqrt{g_0}}\frac{\partial}{\partial x^l}(\sqrt{g_0}hu_t^l)]!^k, \tag{21}$$

$$V_2^k = \{(z_\alpha - \eta)u^l \frac{\partial}{\partial x^l}[\frac{1}{\sqrt{g_0}}\frac{\partial}{\partial x^m}(\sqrt{g_0}hu^m)]\}!^k$$

$$+\frac{1}{2}(z_\alpha^2 - \eta^2)u^l \frac{\partial}{\partial x^l}[\frac{1}{\sqrt{g_0}}\frac{\partial}{\partial x^m}(\sqrt{g_0}u^m)]\}!^k$$

$$+\frac{1}{2}\{[\frac{1}{\sqrt{g_0}}\frac{\partial}{\partial x^l}(\sqrt{g_0}hu^l) + \frac{\eta}{\sqrt{g_0}}\frac{\partial}{\partial x^l}(\sqrt{g_0}u^l)]^2\}!^k, \tag{22}$$

where $k, l, m = 1$ and 2, $(u^1, u^2) = (U, V)$, $(x^1, x^2) = (\xi_1, \xi_2)$; $\frac{\partial}{\partial x_k}$ is the partial derivative, $()_k$ represents the covariant spatial derivative (See Appendix) while $!^k$ represents the contravariant spatial derivative defined as

$$f!^k = \frac{\partial f}{\partial x^i}g^{ik}. \tag{23}$$

3   Numerical method

Numerical analyses (Wei and Kirby 1995) of finite differencing for Boussinesq equations show that it is necessary to adopt high-order schemes in either space or time in Boussinesq equations because the truncation errors of a second-order approximation may contaminate the real dispersive terms in the equations. It also should be noted

9

that the finite differencing on irregular grids can lead to a loss of accuracy if discretizations of the untransformed equations are performed on irregular grids. In the present paper, we can avoid the problem by discretizing the transformed equations in the image domain with regular grids.

By using the tensor formula presented in the Appendix, the system of equations is rewritten in a form that makes the application of the difference procedure convenient as that of Wei et $al.$ (1995). The mass conservation equations (18) and (19) may be expressed as:

$$\eta_t = E(\eta, U, V), \tag{24}$$

where

$$
\begin{aligned}
E = &-\frac{1}{\sqrt{g_0}}\{[\sqrt{g_0}(h+\eta)U]_{\xi_1} + [\sqrt{g_0}(h+\eta)V]_{\xi_2}\} \\
&-\frac{1}{\sqrt{g_0}}\{[a_1 h^2(h+\eta) + \frac{1}{6}\eta(h^2-\eta^2)]\frac{g_{22}}{\sqrt{g_0}}(DU)_{\xi_1} \\
&+[a_2 h(h+\eta) - \frac{1}{2}\eta(h+\eta)]\frac{g_{22}}{\sqrt{g_0}}(DHU)_{\xi_1}\}_{\xi_1} \\
&-\frac{1}{\sqrt{g_0}}\{[a_1 h^2(h+\eta) + \frac{1}{6}\eta(h^2-\eta^2)]\frac{g_{11}}{\sqrt{g_0}}(DU)_{\xi_2} \\
&+[a_2 h(h+\eta) - \frac{1}{2}\eta(h+\eta)]\frac{g_{11}}{\sqrt{g_0}}(DHU)_{\xi_2}\}_{\xi_2} \\
&+\frac{1}{\sqrt{g_0}}\{[a_1 h^2(h+\eta) + \frac{1}{6}\eta(h^2-\eta^2)]\frac{g_{12}}{\sqrt{g_0}}(DU)_{\xi_2} \\
&+[a_2 h(h+\eta) - \frac{1}{2}\eta(h+\eta)]\frac{g_{12}}{\sqrt{g_0}}(DHU)_{\xi_2}\}_{\xi_1} \\
&+\frac{1}{\sqrt{g_0}}\{[a_1 h^2(h+\eta) + \frac{1}{6}\eta(h^2-\eta^2)]\frac{g_{12}}{\sqrt{g_0}}(DU)_{\xi_1} \\
&+[a_2 h(h+\eta) - \frac{1}{2}\eta(h+\eta)]\frac{g_{12}}{\sqrt{g_0}}(DHU)_{\xi_1}\}_{\xi_2},
\end{aligned}
\tag{25}
$$

in which,

$$DU = \frac{1}{\sqrt{g_0}}(\sqrt{g_0}U)_{\xi_1} + \frac{1}{\sqrt{g_0}}(\sqrt{g_0}V)_{\xi_2}, \tag{26}$$

$$DHU = \frac{1}{\sqrt{g_0}}(\sqrt{g_0}hU)_{\xi_1} + \frac{1}{\sqrt{g_0}}(\sqrt{g_0}hV)_{\xi_2}. \tag{27}$$

The momentum equation in ξ_1 direction can be written as

$$\tilde{U}_t = F(\eta, U, V) + [F_1(V)]_t + [F_2(U,V)]_t$$

$$+ F_3(\eta, U_t, V_t) + F_4(\eta, U_t, V_t) + F_5(\eta, U, V) + F_6(\eta, U, V), \tag{28}$$

where

$$\tilde{U} = U + h^2 b_1 \frac{g_{22}}{g_0}[\frac{1}{\sqrt{g_0}}(\sqrt{g_0}U)_{\xi_1}]_{\xi_1} + hb_2 \frac{g_{22}}{g_0}[\frac{1}{\sqrt{g_0}}(\sqrt{g_0}hU)_{\xi_1}]_{\xi_1}, \tag{29}$$

$$F = -\frac{g}{g_0}(g_{22}\eta_{\xi_1} - g_{12}\eta_{\xi_2}) - (UU_{\xi_1} + VU_{\xi_2}$$

$$+ D_{11}^1 U^2 + 2D_{12}^1 UV + D_{22}^1 V^2), \tag{30}$$

$$F_1(V) = -h^2 b_1 \frac{g_{22}}{g_0}[\frac{1}{\sqrt{g_0}}(\sqrt{g_0}V)_{\xi_2}]_{\xi_1}$$

$$- hb_2 \frac{g_{22}}{g_0}[\frac{1}{\sqrt{g_0}}(\sqrt{g_0}hV)_{\xi_2}]_{\xi_1}, \tag{31}$$

$$F_2(U,V) = h^2 b_1 \frac{g_{12}}{g_0}[\frac{1}{\sqrt{g_0}}(\sqrt{g_0}U)_{\xi_1} + \frac{1}{\sqrt{g_0}}(\sqrt{g_0}V)_{\xi_2}]_{\xi_2}$$

$$+ hb_2 \frac{g_{12}}{g_0}[\frac{1}{\sqrt{g_0}}(\sqrt{g_0}hU)_{\xi_1} + \frac{1}{\sqrt{g_0}}(\sqrt{g_0}hV)_{\xi_2}]_{\xi_2}, \tag{32}$$

$$F_3(\eta, U_t, V_t) = \frac{g_{22}}{g_0}[\frac{\eta^2}{2}(DUT) + \eta(DHUT)]_{\xi_1}, \tag{33}$$

$$F_4(\eta, U_t, V_t) = -\frac{g_{12}}{g_0}[\frac{\eta^2}{2}(DUT) + \eta(DHUT)]_{\xi_2}, \tag{34}$$

$$F_5(\eta, U, V) = -\frac{g_{22}}{g_0}[(z_\alpha - \eta)U(DHU)_{\xi_1} + (z_\alpha - \eta)V(DHU)_{\xi_2}$$

$$+ \frac{1}{2}(z_\alpha^2 - \eta^2)U(DU)_{\xi_1} + \frac{1}{2}(z_\alpha^2 - \eta^2)V(DU)_{\xi_2}]_{\xi_1}$$

$$- \frac{1}{2}\frac{g_{22}}{g_0}[((DHU) + \eta(DU))^2]_{\xi_1}, \tag{35}$$

$$F_6(\eta, U, V) = \frac{g_{12}}{g_0}[(z_\alpha - \eta)U(DHU)_{\xi_1} + (z_\alpha - \eta)V(DHU)_{\xi_2}$$

$$+ \frac{1}{2}(z_\alpha^2 - \eta^2)U(DU)_{\xi_1} + \frac{1}{2}(z_\alpha^2 - \eta^2)V(DU)_{\xi_2}]_{\xi_2}$$

$$+ \frac{1}{2}\frac{g_{12}}{g_0}[((DHU) + \eta(DU))^2]_{\xi_2}, \tag{36}$$

in which

$$DUT = \frac{1}{\sqrt{g_0}}(\sqrt{g_0}U_t)_{\xi_1} + \frac{1}{\sqrt{g_0}}(\sqrt{g_0}V_t)_{\xi_2}, \tag{37}$$

11

$$DHUT = \frac{1}{\sqrt{g_0}}(\sqrt{g_0}hU_t)_{\xi_1} + \frac{1}{\sqrt{g_0}}(\sqrt{g_0}hV_t)_{\xi_2}. \tag{38}$$

In equation (28), we introduce $F, F_1, \ldots, F_6$ to represent separately the terms with different properties. F includes the pressure gradient terms and convective terms; F_1 and F_2 are the linear dispersive terms, in which F_2 is the additional term due to the non-orthogonality of the coordinate; F_3 and F_4 are the nonlinear dispersive terms with time derivatives while F_4 is the additional term due to the non-orthogonality; F_5 and F_6 are the nonlinear dispersive terms with spatial derivatives while F_6 is the term due to the non-orthogonality. D^i_{jk} is the Christoffel symbol. The constants a_1, a_2, b_1, b_2 are defined as

$$a_1 = \beta^2/2 - 1/6, a_2 = \beta + 1/2, b_1 = \beta^2, b_2 = \beta \tag{39}$$

where $\beta = z_\alpha/h$, $\beta = -0.531$ in the present paper.

Similarly, the momentum equation in ξ_2 direction can be written as

$$\begin{aligned}
\tilde{V}_t &= G(\eta, U, V) + [G_1(U)]_t + [G_2(U, V)]_t \\
&\quad + G_3(\eta, U_t, V_t) + G_4(\eta, U_t, V_t) + G_5(\eta, U, V) + G_6(\eta, U, V),
\end{aligned} \tag{40}$$

where,

$$\tilde{V} = V + h^2 b_1 \frac{g_{11}}{g_0}[\frac{1}{\sqrt{g_0}}(\sqrt{g_0}V)_{\xi_2}]_{\xi_2} + h b_2 \frac{g_{11}}{g_0}[\frac{1}{\sqrt{g_0}}(\sqrt{g_0}hV)_{\xi_2}]_{\xi_2}, \tag{41}$$

$$\begin{aligned}
G &= -\frac{g}{g_0}(-g_{12}\eta_{\xi_1} + g_{11}\eta_{\xi_2}) - (UV_{\xi_1} + VU_{\xi_2} \\
&\quad + D^2_{11}U^2 + 2D^2_{21}UV + D^2_{22}V^2),
\end{aligned} \tag{42}$$

$$\begin{aligned}
G_1(U) &= -h^2 b_1 \frac{g_{11}}{g_0}[\frac{1}{\sqrt{g_0}}(\sqrt{g_0}U)_{\xi_1}]_{\xi_2} \\
&\quad - h b_2 \frac{g_{11}}{g_0}[\frac{1}{\sqrt{g_0}}(\sqrt{g_0}hU)_{\xi_1}]_{\xi_2},
\end{aligned} \tag{43}$$

$$G_2(U, V) = h^2 b_1 \frac{g_{12}}{g_0}[\frac{1}{\sqrt{g_0}}(\sqrt{g_0}U)_{\xi_1} + \frac{1}{\sqrt{g_0}}(\sqrt{g_0}V)_{\xi_2}]_{\xi_1}$$

12

$$+ h b_2 \frac{g_{12}}{g_0} [\frac{1}{\sqrt{g_0}} (\sqrt{g_0} h U)_{\xi_1} + \frac{1}{\sqrt{g_0}} (\sqrt{g_0} h V)_{\xi_2}]_{\xi_1}, \tag{44}$$

$$G_3(\eta, U_t, V_t) = \frac{g_{11}}{g_0} [\frac{\eta^2}{2} (DUT) + \eta (DHUT)]_{\xi_2}, \tag{45}$$

$$G_4(\eta, U_t, V_t) = -\frac{g_{12}}{g_0} [\frac{\eta^2}{2} (DUT) + \eta (DHUT)]_{\xi_1}, \tag{46}$$

$$G_5(\eta, U, V) = -\frac{g_{11}}{g_0} [(z_\alpha - \eta) U (DHU)_{\xi_1} + (z_\alpha - \eta) V (DHU)_{\xi_2}$$
$$+ \frac{1}{2} (z_\alpha^2 - \eta^2) U (DU)_{\xi_1} + \frac{1}{2} (z_\alpha^2 - \eta^2) V (DU)_{\xi_2}]_{\xi_2}$$
$$- \frac{1}{2} \frac{g_{22}}{g_0} [((DHU) + \eta (DU))^2]_{\xi_2}, \tag{47}$$

$$G_6(\eta, U, V) = \frac{g_{12}}{g_0} [(z_\alpha - \eta) U (DHU)_{\xi_1} + (z_\alpha - \eta) V (DHU)_{\xi_2}$$
$$+ \frac{1}{2} (z_\alpha^2 - \eta^2) U (DU)_{\xi_1} + \frac{1}{2} (z_\alpha^2 - \eta^2) V (DU)_{\xi_2}]_{\xi_1}$$
$$- \frac{1}{2} \frac{g_{12}}{g_0} [((DHU) + \eta (DU))^2]_{\xi_1}. \tag{48}$$

$G, G_1, \dots, G_6$ have the similar meaning as $F, F_1, \dots, F_6$ as described above.

The arrangement of cross-differentiated and nonlinear time-derivative terms on the right hand side of equations (28) and (40) makes the resulting set of left-hand sides purely tridiagonal.

A staggered grid in $\xi_1 - \xi_2$ plane is employed as shown in Figure 2, where the crosses denote η - points at which η is computed, the circles denote U-points at which $\tilde{U}$ and U are computed and the squares denote V-points at which $\tilde{V}$ and V are computed. The separate labeling for η, U and V in this scheme is convenient for the implementation of boundary conditions. The new co-ordinates (ξ_1, ξ_2) are taken as integer grid positions, $\xi_1 = 1, 2, \dots, m, \xi_2 = 1, 2, \dots, n$. Following the work of Wei and Kirby (1995), we discretize the first-order spatial derivative terms to fourth-order accuracy by using standard five-point finite-differencing, leading to truncation errors of $O(\Delta \xi^4)$. The dispersive terms themselves are finite-differenced only to second-order accuracy, leading to error terms of $O(\Delta \xi^2)$ relative to the actual dispersive terms.

13

The fourth-order Adams-Bashforth-Moulton predictor-corrector scheme is employed to perform time updating. A sequence of time instants are defined by $t = p\Delta t$. Level p refers to information at the present, known time level. The predictor step is the third-order explicit Adams-Bashforth scheme, given by

$$\eta_{i,j}^{p+1} = \eta_{i,j}^{p} + \frac{\Delta t}{12}[23(E)_{i,j}^{p} - 16(E)_{i,j}^{p-1} + 5(E)_{i,j}^{p-2}], \tag{49}$$

$$\tilde{U}_{i,j}^{p+1} = \tilde{U}_{i,j}^{p} + \frac{\Delta t}{12}[23(F')_{i,j}^{p} - 16(F')_{i,j}^{p-1} + 5(F')_{i,j}^{p-2}], \tag{50}$$

$$\tilde{V}_{i,j}^{p+1} = \tilde{V}_{i,j}^{p} + \frac{\Delta t}{12}[23(G')_{i,j}^{p} - 16(G')_{i,j}^{p-1} + 5(G')_{i,j}^{p-2}], \tag{51}$$

where

$$F' = F + (F_1)_t + (F_2)_t + F_3 + F_4 + F_5 + F_6, \tag{52}$$

$$G' = G + (G_1)_t + (G_2)_t + G_3 + G_4 + G_5 + G_6. \tag{53}$$

In equations (50) and (51), $(F_1)_t$, $(F_2)_t$, $(G_1)_t$ and $(G_2)_t$ involves time derivatives and the calculation of F_3, F_4, G_3 and G_4 at a certain time level requires the corresponding values of U_t and V_t. They can be evaluated by

$$(w_t)_{i,j}^{p} = \frac{1}{2\Delta t}[3w_{i,j}^{p} - 4w_{i,j}^{p-1} + w_{i,j}^{p-2}] + O(\Delta t^2), \tag{54}$$

$$(w_t)_{i,j}^{p-1} = \frac{1}{2\Delta t}[w_{i,j}^{p} - w_{i,j}^{p-2}] + O(\Delta t^2), \tag{55}$$

$$(w_t)_{i,j}^{p-2} = -\frac{1}{2\Delta t}[3w_{i,j}^{p-2} - 4w_{i,j}^{p-1} + w_{i,j}^{p}] + O(\Delta t^2), \tag{56}$$

where w represents U, V, F_1, F_2, G_1 or G_2.

When $\tilde{U}_{i,j}^{p+1}$ and $\tilde{V}_{i,j}^{p+1}$ are obtained from equations (50) and (51), the contravariant velocity (U, V) at the new time level can be solved by a system of tridiagonal matrix equation, using elimination method.

After the predicted values of $(\eta, U, V)_{i,j}^{p+1}$ are evaluated, the corresponding quantities of $(E, F', G')_{i,j}$ at time levels $(p + 1), (p), (p - 1), (p - 2)$ are obtained. Then we

14

use the fourth-order Adams-Moulton corrector method:

$$\eta_{i,j}^{p+1} = \eta_{i,j}^{p} + \frac{\Delta t}{24}[9(E)_{i,j}^{p+1} + 19(E)_{i,j}^{p} - 5(E)_{i,j}^{p-1} + (E)_{i,j}^{p-2}], \qquad (57)$$

$$\tilde{U}_{i,j}^{p+1} = \tilde{U}_{i,j}^{p} + \frac{\Delta t}{24}[9(F')_{i,j}^{p+1} + 19(F')_{i,j}^{p} - 5(F')_{i,j}^{p-1} + (F')_{i,j}^{p-2}], \qquad (58)$$

$$\tilde{V}_{i,j}^{p+1} = \tilde{V}_{i,j}^{p} + \frac{\Delta t}{24}[9(G')_{i,j}^{p+1} + 19(G')_{i,j}^{p} - 5(G')_{i,j}^{p-1} + (G')_{i,j}^{p-2}]. \qquad (59)$$

Similar to the treatment in the predictor stage, $U_t, V_t, (F_1)_t, (F_2)_t, (G_1)_t$ and $(G_2)_t$ are evaluated in the following manner:

$$(w_t)_{i,j}^{p+1} = \frac{1}{6\Delta t}(11w_{i,j}^{p+1} - 18w_{i,j}^{p} + 9w_{i,j}^{p-1} - 2w_{i,j}^{p-2}) + O(\Delta t^3), \qquad (60)$$

$$(w_t)_{i,j}^{p} = \frac{1}{6\Delta t}(2w_{i,j}^{p+1} + 3w_{i,j}^{p} - 6w_{i,j}^{p-1} + w_{i,j}^{p-2}] + O(\Delta t^3), \qquad (61)$$

$$(w_t)_{i,j}^{p-1} = -\frac{1}{6\Delta t}(2w_{i,j}^{p-2} + 3w_{i,j}^{p-1} - 6w_{i,j}^{p} + w_{i,j}^{p+1}] + O(\Delta t^3), \qquad (62)$$

$$(w_t)_{i,j}^{p-2} = -\frac{1}{6\Delta t}(11w_{i,j}^{p-2} - 18w_{i,j}^{p-1} + 9w_{i,j}^{p} - 2w_{i,j}^{p+1}) + O(\Delta t^3). \qquad (63)$$

The corrector step is iterated until the error between two successive results reaches a required\limit. The error is computed for each of the three dependent variables η, U, V and is defined as in Wei *et al.* (1995):

$$\Delta f = \frac{\sum_{i,j} |f_{i,j}^{p+1} - f_{i,j}^{(p+1)^*}|}{\sum_{i,j} |f_{i,j}^{p+1}|}, \qquad (64)$$

where f denotes η, U or V and $()^*$ denotes the previous results. The corrector step is iterated if any of the Δf exceeds 10^{-4}.

Initial testing of the present staggered-grid scheme has shown it to be a considerable improvement over the scheme of Wei and Kirby (1995), in terms of short wave length noise generation. A more extensive exploration of the behavior of the two schemes is underway and will be reported separately.

4 Boundary conditions

For computations of wave propagation in domains with complicated boundaries, appropriate boundary conditions have to be specified in the numerical model. Generally, for a perfectly reflected vertical wall, the horizontal volume flux normal to the wall is zero. Wei and Kirby (1995) derived a set of boundary conditions satisfied by normal velocity at z_α, tangential velocity and surface elevation by considering only the leading order terms in the mass conservation equation. i.e., for the case of a vertical wall parallel to x axis , the boundary conditions are

$$v = 0; \quad \eta_y = 0; \quad u_y = 0. \tag{65}$$

They then applied five-point off-center finite difference to the equations above. These boundary conditions may be adopted in curvilinear coordinates if we use the contravariant component (U, V) instead of (u, v). That is

$$U = 0; \quad at \quad \Pi_1, \Pi_2, \tag{66}$$

$$V = 0; \quad at \quad \Pi_3, \Pi_4, \tag{67}$$

$$\eta!^1 = 0; \quad V!^1 = 0 \quad at \quad \Pi_1, \Pi_2, \tag{68}$$

$$\eta!^2 = 0; \quad U!^2 = 0 \quad at \quad \Pi_3, \Pi_4. \tag{69}$$

The boundary conditions (66) and (67) can be easily obtained in the staggered grids because U points are located on Π_1, Π_2 and V points on Π_3, Π_4. The symmetric or anti-symmetric conditions are used to apply the boundary conditions, i.e., U values are anti-symmetric to Π_1 and Π_2, V values are anti-symmetric to Π_3 and Π_4 according to (66) and (67), while U and η values are symmetric to Π_3 and Π_4, V and η values

16

are symmetric to Π_1 and Π_2 according to (68) and (69). The symmetric or anti-symmetric conditions also make it easy to discretize equations on boundaries or in the vicinity of boundaries, especially for high order finite differences with five-point schemes.

The sponge layer boundary condition and the wave generating boundary condition are also implemented in this paper following Wei and Kirby (1995).

5   Examples

5.1   Wave evolution in a rectangular basin

As a simple yet efficient test case (Wei and Kirby, 1995), the evolution of waves in a rectangular basin was calculated by using both the uniform rectangular grid model and the curvilinear grid model. Though there are no corresponding nonlinear analytical solutions or experimental data to compare with, the comparison between the results from the two models can show a consistency of the solutions on curvilinear grids and rectangular grids.

The basin dimensions are $20m \times 20m$, and the water depth is $0.5m$ constant over the basin. The initial condition is provided by a motionless Gaussian hump of water with its center located at the center of the basin (x_c, y_c):

$$\eta(x, y, t = 0) = H_0 \exp\{-\gamma[(x - x_c)^2 + (y - y_c)^2]\}, \tag{70}$$

$$u(x, y, t = 0) = 0, \tag{71}$$

$$v(x, y, t = 0) = 0, \tag{72}$$

where H_0 is the initial height of the hump, γ is the shape coefficient, and (x_c, y_c) is the coordinate at the center of the domain. We chose $H_0 = 0.2m$, $\gamma = 0.4$, and

17

$x_c = y_c = 10m$.

In the rectangular grid model, grid sizes are set to be identical everywhere as $\Delta x = \Delta y = 0.1m$. For the curvilinear grid model, a grid generation method (Brackbill, 1982) can be used to generate the curvilinear grid. As a test, we generate a curvilinear grid by weighting the center point as shown in Figure 3 in which the maximum grid size is $0.15m$ near boundaries, while the minimum grid size is $0.045m$ at the center of the domain. The total number of grid points is 200×200, as the same as that of the regular grid model.

Figure 4 shows water surface contour in the physical domain and the contour obtained from the rectangular model. There is very small difference between the dashed line and the solid line in Figure 4. The small differences are caused by the interpolation errors and by the different resolutions of the initial Gaussian hump. Numerical experiments show that the difference decreases with a reduction of grid sizes in both models.

5.2   Monochromatic waves shoaling on a slope

As a second example using the coordinate-stretching approach, we study periodic wave propagation over a sloping beach where there is a contraction of the wavelength and a resulting increase in required resolution as waves shoal towards shore. The previous uniform grid model generally makes the computation expensive because fine grids with constant grid spacing are always adopted in order to resolve short waves in shallow water, and further, the time step needs to be small in order to have an appropriate Courant number in deep water. The problem can be solved by using an irregular grid in which the grid spacing is adjusted according to the water depth so that the Courant number in each element is constant in the whole domain. The

idea has been used by Kashiyama and Okada (1992) in shallow water flow analysis. To show the efficiency of the present model in dealing with wave propagation over a sloping beach, we present a 1-D model with the stretched grid size in the present case.

Figure 5 shows a mild-slope beach, where a constant depth of $8m$ on the left connects to a constant slope on the right. Waves with a period of $4s$ are generated by a wavemaker located on the left side. Two sponge layers are placed at both ends of the domain to absorb wave energy. The uniform grid model and the stretched grid model are then used respectively in this case.

In the uniform grid model, a constant grid size of $0.4m$ is adopted, giving a total of 2500 grid points in the computation domain. According to linear theory, the corresponding wavelength in the deepest water is $45.2m$, while shortest wavelength in the shallow water is $18.4m$. Thus there are 46 grid points per wavelength in the shallowest region on the right side and 113 grid points per wavelength in the deepest water region on the left side. The choice of an adequate resolution in shallow water thus leads to an over-resolution of the wave form in deep water. In addition, for a given time step, the Courant number increases with the increase of water depth. Therefore, a time step has to be selected according to the Courant number in deep water. Here, the time step in the uniform grid model is chosen to be $0.025s$ which leads to the Courant number of 0.19 in the shallowest region and 0.471 in the deepest region.

In the stretched grid model, gradually varying grid sizes are chosen from $1m$ in the deepest region to $0.40m$ in the shallowest region according to the following coordinate transformation:

$$\xi = A\frac{x}{C} \tag{73}$$

19

where C is the wave celerity from the linearized Boussinesq equations and A is a coefficient, $A = 7.52$ in this case. The Courant number is constant in the whole computational domain. The total grid number decreases to 1420, 43% less than that of the uniform grid model. Even so, the resolution of the model is not reduced since there are 45 grid points per wavelength both in deep water and in shallow water, comparing to the 46 points per wavelength in shallow water in the uniform grid model. The time step for the stretched grid model can be much larger than that for uniform grid model because of the larger grid spacing in deeper water. For instance, the time step in this case is chosen to be $0.06s$, which is 2.4 times larger than that in uniform grid model and gives a Courant number of 0.452. The decrease in grid number and increase in time step make the stretched grid model much more efficient in comparison with the uniform grid model. In such a case, more than a four time speed-up may usually be expected in view of the grid numbers and time steps used in the two different models. The actual computational time in the stretched grid model is 3.1 times faster than the uniform grid model, which is a little slower than expected because the stretched grid model needs a few more iterations in the calculation. In the computation of wave propagation on a natural beach with a relatively mild slope offshore and a steep slope close to the shore line, the efficiency will be more obvious.

The surface elevations obtained from the stretched grid model are presented in the image domain as shown in Figure 6. It is clear that the wavelength in the image plane is almost constant, which illustrates that the model provides the same resolution when waves propagate from deep water to shallow water. The surface elevations in the physical domain are shown in figure 7 in comparison with the results from the uniform grid model. Figures 8 and 9 respectively display the comparisons of wave height and wave number between the two models. The wave numbers here are obtained from

20

the wave elevation distributions calculated in the two models. The comparisons show that the stretched grid model results are in good agreement with results from the uniform grid model.

5.3 Waves in a circular channel

The present example is a constant depth channel with vertical sidewalls laid out in a circular planform. Dalrymple *et al.* (1994) used spectral methods with coordinate-transformed equations to analytically study linear wave propagation. In their study, three cases with different widths of channel, namely, narrow, wider and very wide channels, were carried out. The case of the very wide channel presents a more complicated pattern of waves with diffraction and strong reflection. Thus, this case is chosen for study in this paper, and comparison is made between the numerical results and analytic solution.

Let r_1 and r_2 be the inner and outer radius of the channel respectively, with $r_1 = 75m, r_2 = 200m$ in this case. The depth of the channel is $4m$. The coordinate transformation can be described as:

$$\xi_1 = \frac{\sqrt{x^2 + y^2}}{r_2 - r_1} \tag{74}$$

$$\xi_2 = \frac{1}{\pi} tan^{-1}(\frac{y}{x}) \tag{75}$$

The grid mesh in the physical domain is shown in Figure 10. The grid spacing in the radial direction is constant at $1m$, while a constant angular grid is used along the channel length, resulting in a maximum tangential grid size of $1.26m$ near the outer wall and a minimum of $0.47m$ near the inner wall. The waves propagate primarily counter-clockwise from the mouth of the channel. A wavemaker is located internally at the eastern end of the channel and two sponge layers are placed in straight channels

21

extending from the eastern and western end of the circular channel (not shown in Figure 10). The wavemaker produces linear waves with a period of $4s$ and a very small amplitude for comparison with the linear analytic solution. The time step is chosen as $0.05s$ in the present case.

To illustrate the process of wave propagation in the channel, Figures 11 - 13 show the transient propagation of a wave train into the channel. It is shown that the waves initially propagate in a straight line, but as the channel bends, the waves start to diffract around the bend and simultaneously run into the curving channel sidewall and are reflected around the bend. The present method allows for transient wave propagation while the spectral method given by Dalrymple *et al.* can only describe a steady-state linear solution. Figures 14 and 15 depicted the comparisons of the water surface variation along outer wall and inner wall between the analytic solution and numerical solution after a periodic steady state has been achieved. Good agreements are found in the comparisons.

5.4 Diffraction of a solitary wave by a straight vertical wall

An experiment on the diffraction of a solitary wave by a straight thin wall was carried out by Perroud (1957) in a wave tank. A diffracting wall of $0.8cm$ thickness is placed in the tank to diffract the solitary wave at normal incidence. Figure 16 shows the experiment layout, where the measurements were made at a point (ρ, θ) in the defined polar coordinate. The tests were run at a constant water depth of $6.1cm$ and various ratios, ranging from 0.27 to 0.58, of the incident wave height to water depth. Measurements of wave heights and patterns of the diffracted waves were performed in different directions θ from the diffracting wall and the central axis at the distance ρ.

22

To simulate the diffraction of waves in the experiment, it is necessary to use stretched grid model to resolve the thin diffraction wall. Thus a stretched rectangular grid mesh is generated in the computation domain with linear variation of grid sizes along the axis direction. The finest grids are obtained around the wall with the smallest grid size of $0.8cm$, which is exactly the thickness of the wall. The largest grid size in the whole domain is $2.54cm$ ($1in$) at the two sides of the domain. The grid size in the normal direction of the axis is identical as $2.54cm$. The location of initial solitary wave is set at $76.2cm$ eastward from the wall.

The diffraction and reflection process after an incident solitary wave impacts on the wall is shown in a time sequence of contour plots of the surface elevation for the case of $a_0/h = 0.42$ (Figure 17). When the wave impinges on the wall ($t = 0.8s$), the wave on the upward side runs up and reflects back. The initial development of the diffracted wave can be clearly seen near the tip of the wall. Following the wave impact, the early stages of propagation of the diffracted solitary wave and the backscattered reflected wave are then shown at $t = 0.9s$. At $t = 1.4s$, the initial primary wave separates into a forward transmitted diffracted wave and a backward scattered reflected wave. The newly evolved secondary backscattered and forward-scattered waves generated from the tip of the wall propagated outward and follow the leading reflected and diffracted waves, respectively.

The numerical results and measurement data obtained from four solitary waves with different wave heights are compared in Figure 18(a)-(h). The diffraction coefficient k, defined as the ratio of the diffracted wave height to the incident wave height (a/a_0), is plotted against the distance ρ for different values of the angle θ. The close agreement proves that the present model is capable of simulating nonlinear wave propagation.

23

5.5 Application to Ponce de Leon Inlet

To demonstrate the practicality of the present model, we use the model to simulate the propagation of monochromatic waves in Ponce de Leon Inlet, Florida, USA. Smith and Harkins (1997) used numerical models to estimate wave transformation over Ponce de Leon Inlet and comparisons were made between numerical results and measurement data from the physical model. The geometry is shown in Figure 19, which consists of a coastline, a jetty, an inlet leading to the Halifax and Indian Rivers, and a complex bathymetry. A boundary-fitted grid is generated as shown in Figure 20. In order to resolve structures and short waves in shallow water, finer resolution is used near the jetty, coastal lines and the inlet. At the offshore boundary of the domain, monochromatic waves are generated with a period of $15s$ and a small amplitude. To avoid wave reflections by the coastal boundaries and wave breaking in shallow water, sponge layers are placed in shallow water area along the coastlines. Figure 21 shows a snapshot of surface elevations, showing wave reflection on the upward side of the jetty, wave diffraction on the leeward side, refractive wave focusing in the area to the right of the inlet mouth, and standing waves inside the inlet. Though the numerical results have not been compared with measurement data as there is no consideration of energy dissipation by wave breaking and wave runup on sloping beaches yet, this case study illustrates that the present model has a potential prospect for computations in complicated domains, such as in harbors and tidal inlets.

6 Conclusions

Based on the fully nonlinear Boussinesq equations derived by Wei *et al.* (1995), the equations in generalized curvilinear coordinates are derived by using contravariant

velocity method. Then the numerical model is developed with a high-order finite difference scheme in staggered grids. To test the model, five examples involving curvilinear or stretched coordinate systems are applied. The computation of wave evolution in a rectangular basin with a curvilinear grid indicates that the model is consistent with the uniform grid model. In the case of wave propagation on a sloping beach, the same element Courant number is obtained in every grid points by adjusting the grid size, so that the resolutions of waves are the same both in shallow water and deep water. The computational efficiency is shown to be greatly improved by the new model. Wave propagation in a circular channel is simulated by employing the present model with the boundary-fitted grid. Good agreement is found between the numerical results and analytic solution. Then the model is used to simulate the diffraction of a solitary wave by a straight vertical wall at normal incidence. The comparison between numerical results and measurements shows that the model has good accuracy in dealing with the computation of nonlinear wave propagation with complex lateral boundaries. Finally, the model is applied to Ponce de Leon Inlet. In this case, monochromatic waves are simulated in the complex-shaped domain with a real bathymetry.

For practical application in complicated domains, the present model needs to be further improved with the incorporation of energy dissipation by wave breaking and wave runup on sloping beaches and structures. The development will be reported on in the near future, in conjunction with a more complete investigation of Ponce de Leon Inlet.

Acknowledgements

References

Abbott, M. B., Petersen, H. M., Skovgaard, O., 1978, Numerical modeling of short waves in shallow-water, J Hydraul. Res. 16(3), 173-204.

Abbott, M. B., McCowan, A.D. and Warren, I. R., 1984, Accuracy of short-wave numerical model, J. Hydr. Engng, 110, 1287-1301.

Borthwick, A. G. L. and Barber, R. W., 1992, River and reservoir flow modeling using the transformed shallow water equations, Int. J. Numer. Methods Fluids, 14, 1193-1217.

Chen, C, Zheng, L. and Zhu, J., 1999, A non-orthogonal primitive equation coastal ocean circulation model, submitted to Journal of Atmospheric and Oceanic Technology.

Chen, Q., Kirby, J. T., Dalrymple, R. A., Kennedy, A., and Chawla, A., 1999a, Boussinesq modeling of wave transformation, breaking and runup. II: 2D, J. Waterway, Port, Coastal and Ocean Engrng., in press.

Chen, Q., Dalrymple, R.A., Kirby, J. T., Kennedy, A. and Haller M. C., 1999b, Boussinesq modeling of a rip current system, Journal of Geophysical Research, in press.

Dalrymple R. A., Kirby, J. T. & Martin, P. A., 1994, Spectral methods for forward-propagating water waves in conformally-mapped channels, Applied Ocean Re-

search, 16, 249-266.

Elgar, S. & Guza, R. T., 1985, Shoaling gravity waves: comparisons between field observations, linear theory and a nonlinear model, J. Fluid Mech., 158, 47-70.

Goring, D. G., 1978, Tsunamis - the propagation of long waves onto a shelf, PhD dissertation, California Institute of Technology, Pasadena, California.

Häuser, J., Paap, H. G., Eppel, D. and Mueller, A., 1985, Solution of shallow water equations for complex flow domains via boundary fitted coordinates, Int. J. Numer. Methods Fluids, 5, 727-744.

Häuser, J., Paap, H. G., Eppel, D. and Sengupta, S., 1986, Boundary conformed coordinate systems for selected two-dimensional fluid flow problems. Part 2: Application of the BFG method, Int. J. Numer. Methods Fluids, 6, 529-539.

Isobe, M., 1986, A parabolic refraction-diffraction equation in the ray-front coordinate system, Proc. 20th Intl. Conf. Coastal Engrg., Taipei, 306-317.

Kaku, H. and Kirby, J. T., 1988, A parabolic equation method in polar coordinates for waves in harbors, Tech. Rept. UFL/COEL-TR/075, Coastal and Oceanographic Engrg. Dept., Univ of Florida, Gainesville, Fla.

Kashiyama, K. and Okada, T., 1992, Automatic mesh generation method for shallow water flow analysis, Int. J. Numer. Methods Fluids, 15, 1037-1057.

Kennedy, A. B, Chen, Q., Kirby, J. T., and Dalrymple, R. A., 1999, Boussinesq modeling of wave transformation, breaking and runup. I: 1D, J. Waterway, Port, Coastal and Ocean Engrng., in press.

Kirby, J. T., 1988, Parabolic wave computations in non-orthogonal coordinate systems, Journal of Waterway, Port, Coastal and Ocean Engineering, 114, 673-685.

Kirby, J. T., Dalrymple, R. A. and Kaku, H., 1994, Parabolic approximations for water waves in conformal coordinate systems, Coastal Engineering, 23, 185-213.

Liu, P. L.-F., Yoon, S. N. & Kirby, J. T., 1985, Nonlinear refraction-diffraction of waves in shallow water, J. Fluid Mech., 153, 184-201.

Liu, P. L.-F. and Boissevain, P., 1988, Waves propagation between two breakwater, J. Waterway, Port, Coastal and Ocean Engineering, 114(2), 237-347.

Madsen, P. A., Murray, R. & Sørensen, O. R., 1991, A new form of Boussinesq equations with improved linear dispersion characteristics, Coastal Engineering, 15, 371-388.

Nwogu, O., 1993, An alternative form of the Boussinesq equations for nearshore wave propagation, J. Waterway, Port, Coast, Ocean Engng., 119, 618-638

Peregrine, D. H., 1967, Long waves on a beach, J. Fluid Mech., 27, 815-827.

Perroud P. H., 1957, The solitary wave reflection along a straight vertical wall at oblique incidence, Technical Report Series 99, Issue 3, Institute of Engineering Research, University of California, Berkeley, CA.

Raghunath, R., Sengupta, S. and Häuser, J., 1987, A study of the motion in rotating containers using a boundary-fitted coordinate system, Int. J. Numer. Methods Fluids, 7, 453-464.

Rygg, O. B., 1988, Nonlinear refraction-diffraction of surface waves in intermediate and shallow water, Coastal Engineering, 12, 191-211.

Sheng, Y. P., 1986, Modeling coastal and estuarine processes using boundary-fitted grids, Proceedings 3rd Int'l Symposium on River Sedimentation, 1416-1442.

Shi, F. and Sun, W., 1995, A variable boundary model of storm surge flooding in generalized curvilinear coordinate grids, Int. J. Num. Methods Fluids, 21, 641-651.

Shi, F. and Zheng, L., 1996, A BFG model for calculation of tidal current and diffusion of pollutants in nearshore areas, Acta Oceanologica Sinica, 15(2), 283-296.

Shi, F., Sun, W. and Wei, G., 1997, A WDM method on generalized curvilinear grid for calculation of storm surge flooding, Applied Ocean Research, 19, 275-282.

Shi, F., Kong, Y. and Ding, P., 1998, An implicit method using contravariant velocity components and calculations in a harbor-channel area, Acta Oceanologica Sinica, 20(4), 17-24.

Smith, S. J. and Harkins, G. S., 1997, Numerical wave model evaluations using laboratory data, Ocean wave measurement and analysis, vol 1, 271-285.

Tsay, T.-K. and Liu, P. L.-F., 1982, Numerical solution of water wave refraction and diffraction problems in the parabolic approximation, J. Geophys. Res. 87, 7932-7940.

Wang, K. H., Wu, T. Y. & Yates, G. T., 1992, Three-dimensional scattering of solitary waves by vertical cylinder, J. Waterway, Port, Coast and Ocean Engineering, 118, 551-556.

Warsi, Z. U. A., 1998, **Fluid Dynamics: Theoretical and Computational Approaches**, 2nd ed. CRC Press, New York.

Wei, G. & Kirby, J. T., 1995, A time-dependent numerical code for the extended Boussinesq equations, J. Waterway, Port, Coastal and Ocean Engineering, 121, 5, 251-261.

Wei, G. & Kirby, J. T., Grilli, S. T. and Subramanya, R., 1995, A fully nonlinear Boussinesq model for surface waves, Part 1, Highly nonlinear unsteady waves, J. Fluid Mech., 294, 71-92.

Wei, G. & Kirby, J. T., 1998, Simulation of water waves by Boussinesq model, Research Report No. CACR-98-02, Center for Applied Coastal Research, University of Delaware.

Appendix: Spatial derivative in tensor forms

The tensor-invariant forms of controlling equations (18) - (22) can be expanded into equations (24) - (48) by using the following tensor formulas.

The gradient of a scalar f can be written as:

$$\nabla f = \frac{\partial f}{\partial x^i} \mathbf{g}^i \qquad (76)$$

where $\mathbf{g}^i$ is the contravariant basis. According to the relationship between two different basis:

$$\mathbf{g}^i = g^{ij} \mathbf{g}_j \qquad (77)$$

in which g^{ij} is the contravariant metric, the gradient can be expressed on the covariant basis $\mathbf{g}_i$ as

$$\nabla f = \frac{\partial f}{\partial x^i} g^{ij} \mathbf{g}_j = f^{!j} \mathbf{g}_j \qquad (78)$$

In the present paper, for example, since the contravariant velocity is introduced as the dependent variable, the equations have to be expended on the covariant basis $\mathbf{g}_i$.

The pressure gradient term may be expressed as

$$
\begin{aligned}
\nabla \eta &= \eta^{!i} \mathbf{g}_i \\
&= (g^{11}\frac{\partial \eta}{\partial \xi_1} + g^{21}\frac{\partial \eta}{\partial \xi_2})\mathbf{g}_1 + (g^{12}\frac{\partial \eta}{\partial \xi_1} + g^{22}\frac{\partial \eta}{\partial \xi_2})\mathbf{g}_2 \\
&= \frac{1}{g_0}(g_{22}\frac{\partial \eta}{\partial \xi_1} - g_{12}\frac{\partial \eta}{\partial \xi_2})\mathbf{g}_1 + \frac{1}{g_0}(-g_{12}\frac{\partial \eta}{\partial \xi_1} + g_{11}\frac{\partial \eta}{\partial \xi_2})\mathbf{g}_2
\end{aligned}
\tag{79}
$$

where g_0 is the determinant of the metric tensor. In equation(79), we employed the following formula:

$$
g_{ik}g^{jk} = \delta_i^j
\tag{80}
$$

where δ_i^j is the Kronecker delta.

The divergence of a vector $\mathbf{u}$ can be written as

$$
\nabla \cdot \mathbf{u} = \frac{1}{\sqrt{g_0}}\frac{\partial \sqrt{g_0}u^i}{\partial x^i}
\tag{81}
$$

In the present paper, $\nabla \cdot \mathbf{u}$ can be expanded as

$$
\begin{aligned}
\nabla \cdot \mathbf{u} &= \frac{1}{\sqrt{g_0}}\frac{\partial}{\partial x^i}\left(\sqrt{g_0}u^i\right) \\
&= \frac{1}{\sqrt{g_0}}\frac{\partial \sqrt{g_0}U}{\partial \xi_1} + \frac{1}{\sqrt{g_0}}\frac{\partial \sqrt{g_0}V}{\partial \xi_2},
\end{aligned}
\tag{82}
$$

where U and V are the contravariant components of velocity vector.

To a vector $\mathbf{u}$ in a two-dimensional space, the covariant spatial derivative $u^i_{,j}$ can be expressed in terms of the contravariant component u^i of $\mathbf{u}$ as following

$$
u^i_{,j} = \frac{\partial u^i}{\partial x^j} + u^k D_{jk}^i
\tag{83}
$$

where D_{jk}^i is the Christoffel symbol. Then the convective terms in the paper can be expanded as follows:

$$
\begin{aligned}
u^l u^1_{,l} &= u^1 u^1_{,1} + u^2 u^1_{,2} \\
&= U\frac{\partial U}{\partial \xi_1} + V\frac{\partial U}{\partial \xi_2} + UUD_{11}^1 + 2UVD_{12}^1 + VVD_{22}^1,
\end{aligned}
\tag{84}
$$

31

$$u^l u^2_{,l} = u^1 u^2_{,1} + u^2 u^2_{,,2}$$

$$= U\frac{\partial V}{\partial \xi_1} + V\frac{\partial V}{\partial \xi_2} + UUD^2_{11} + 2UVD^2_{12} + VVD^2_{22}. \tag{85}$$
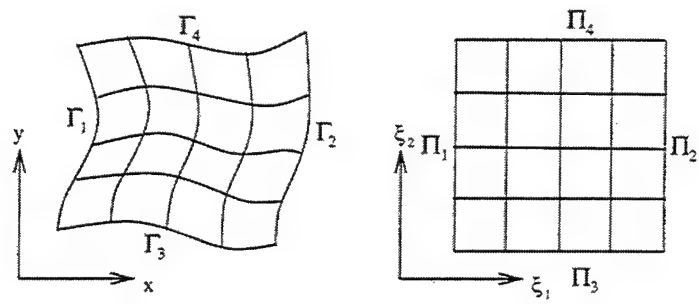
Figures

Figure 1: Physical domain (x, y) and transformed image domain (ξ_1, ξ_2).
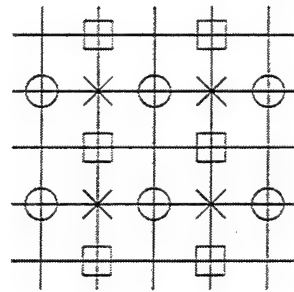
Figure 2: Staggered grid in the image domain($\times - \eta$- point , $\bigcirc - U$- point and $\square -$ V- point).
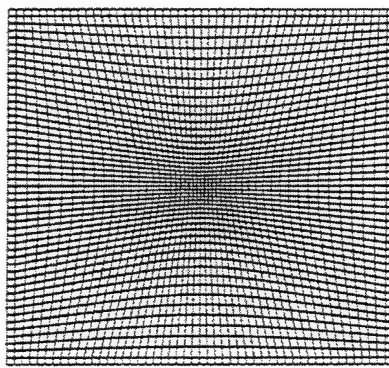
Figure 3: Curvilinear grid for rectangular basin experiment.
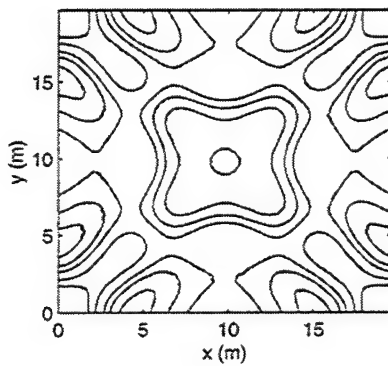
Figure 4: Comparison of surface elevations $(t = 8s)$ in the physical domain between regular grid model (solid line) and curvilinear grid model (dashed line).
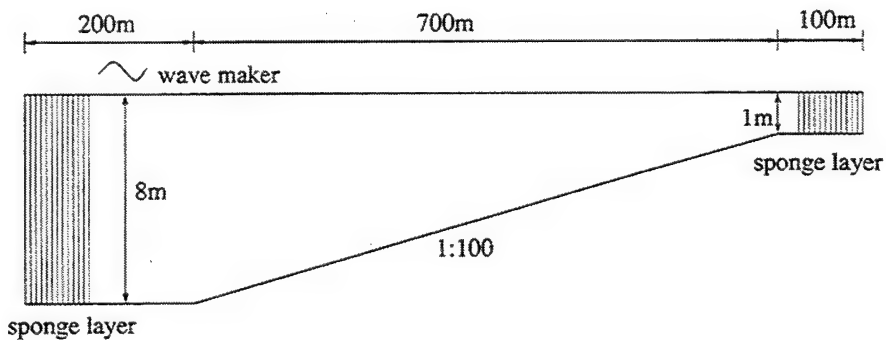
Figure 5: Schematic of the wave flume.
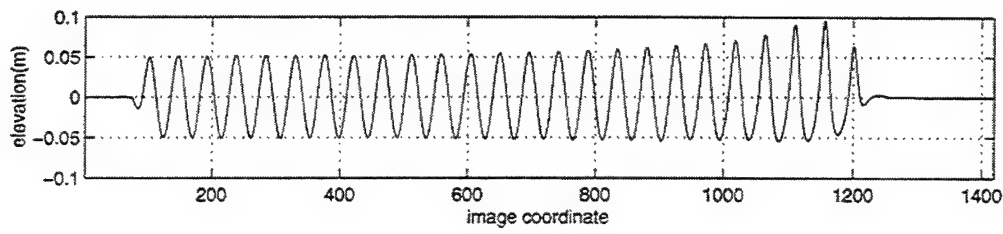
Figure 6: The stretched grid model: surface elevations in the image domain.
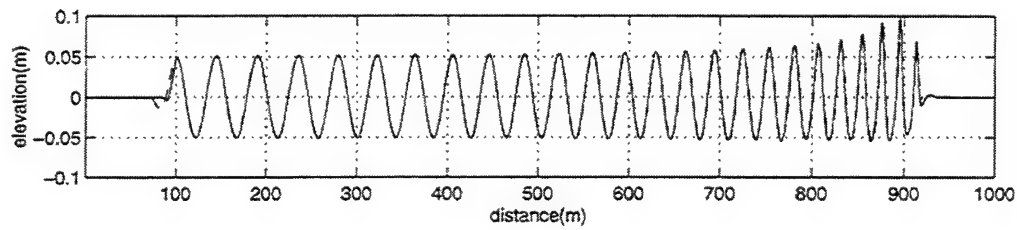
Figure 7: Surface elevation comparison between the uniform grid model (solid line) and the stretched grid model (dashed line) in the physical domain.
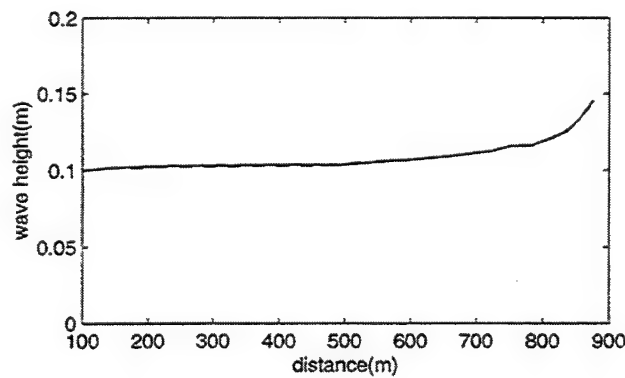
Figure 8: Comparison of wave heights between uniform grid model (solid line) and stretched grid model (dashed line).

35
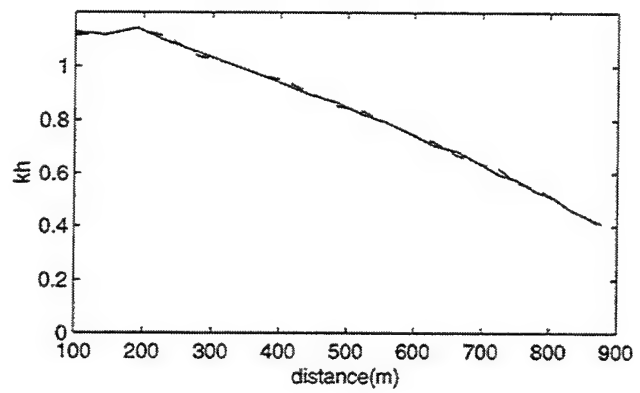
Figure 9: Comparison of wave numbers between uniform grid model (solid line) and stretched grid model (dashed line).
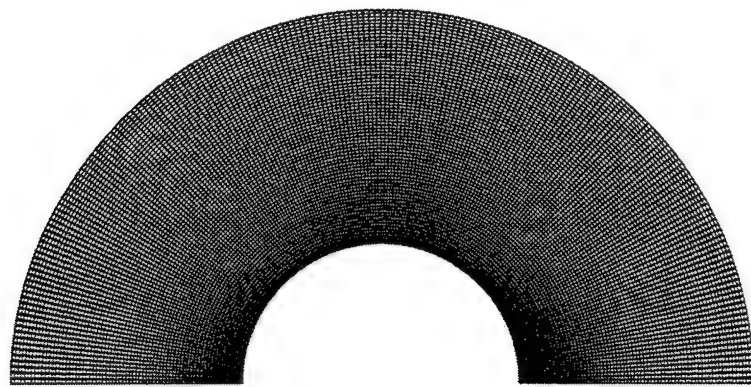
Figure 10: Calculation grid in the circular channel.
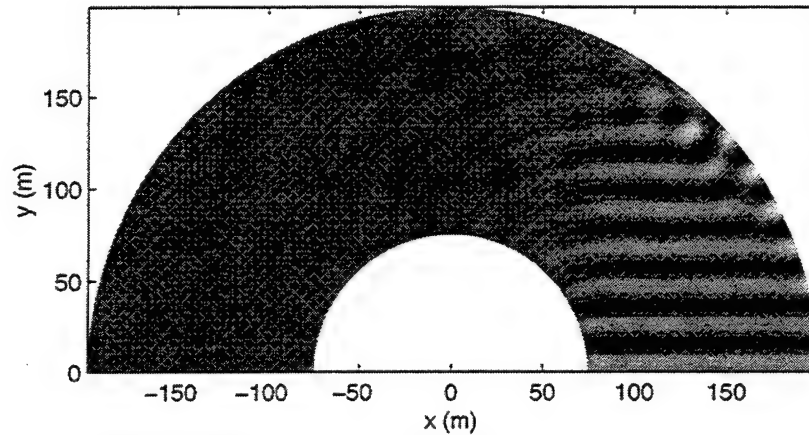
Figure 11: Wave propagation in the circular channel(t= 50 seconds).
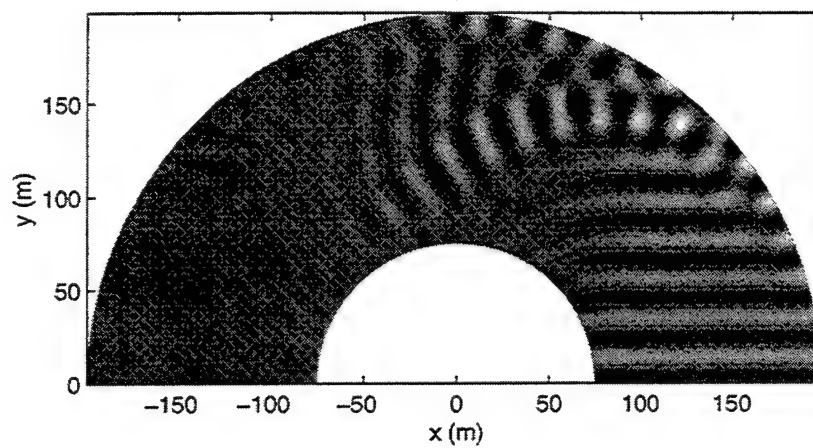
Figure 12: Wave propagation in the circular channel(t= 100 seconds).
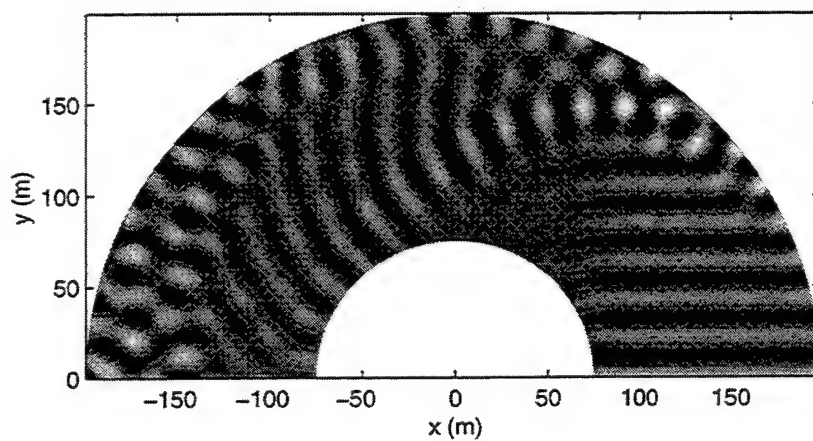
Figure 13: Wave propagation in the circular channel(t= 200 seconds).
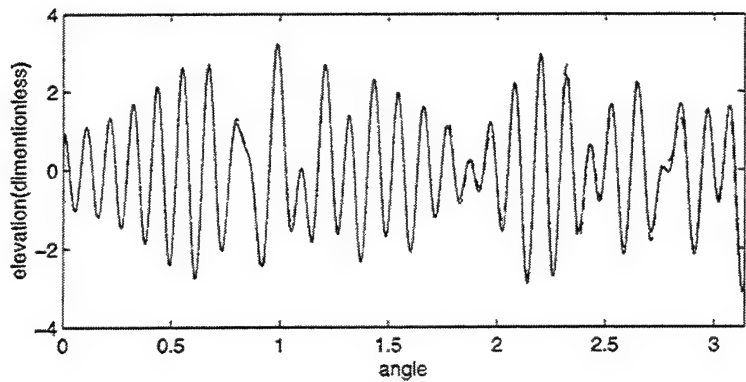
Figure 14: Comparison of the surface variation along outer wall between the analytic solution(solid line) and numerical solution(dashed line).
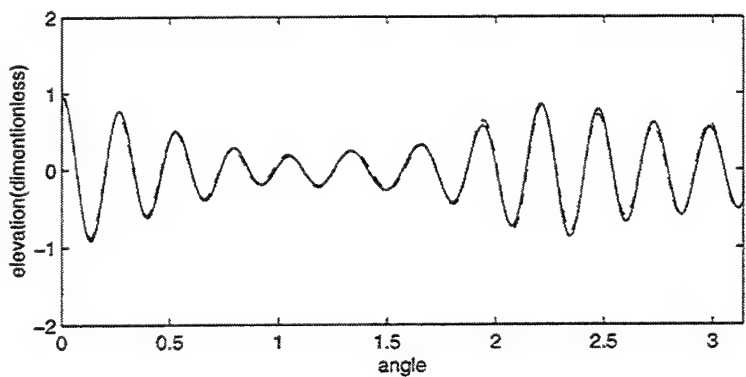

Figure 15: Comparison of the surface variation along inner wall between the analytic solution(solid line) and numerical solution(dashed line).
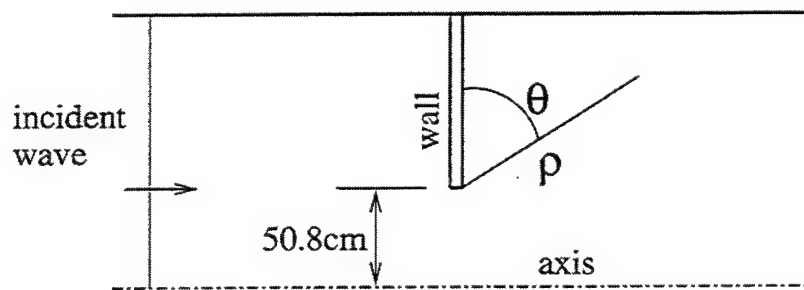
Figure 16: Experimental layout.
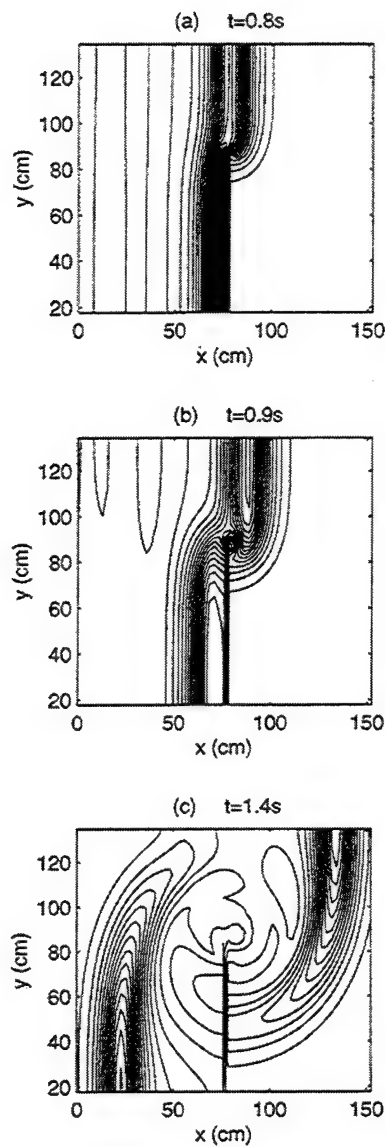
Figure 17: Contour plots of surface elevation for $a_0/h = 0.42$ at various times.
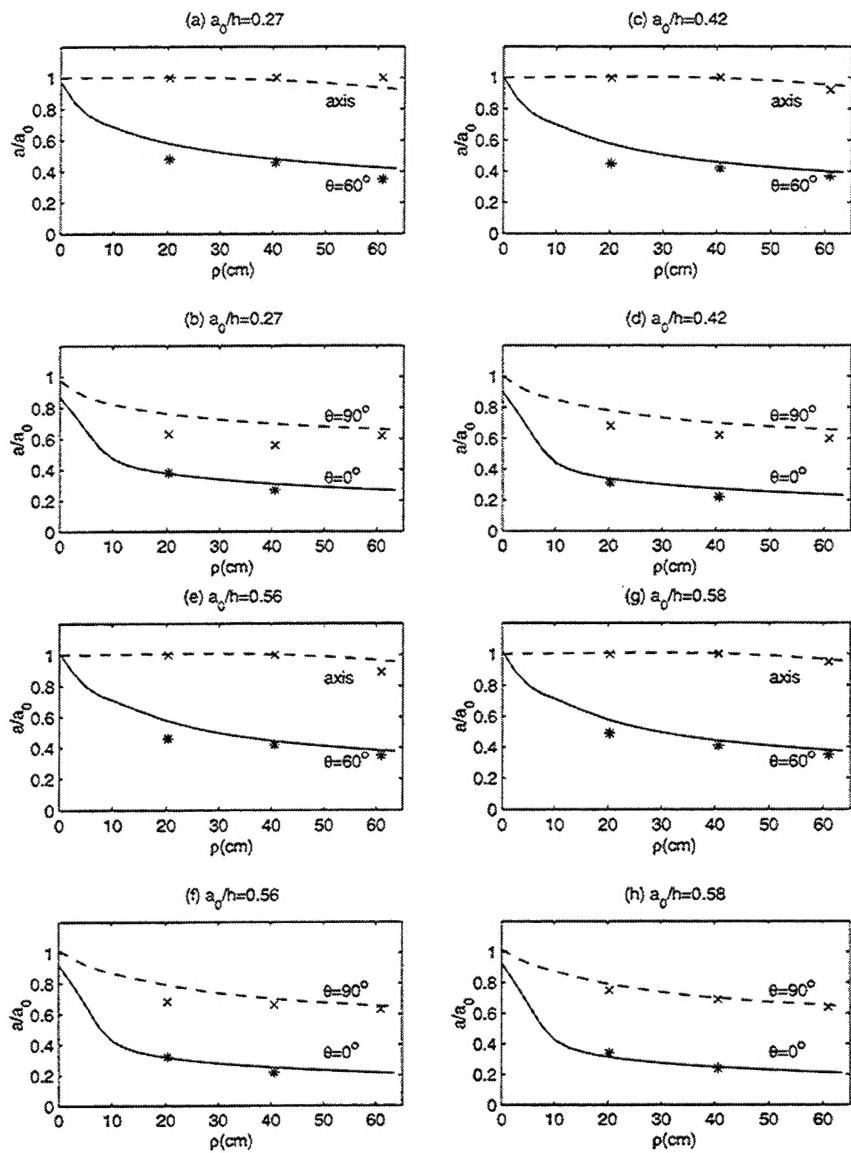
Figure 18: Comprisons of diffraction coefficients between experimental data(∗ or ×
) and numerical results(solid or dashed lines)
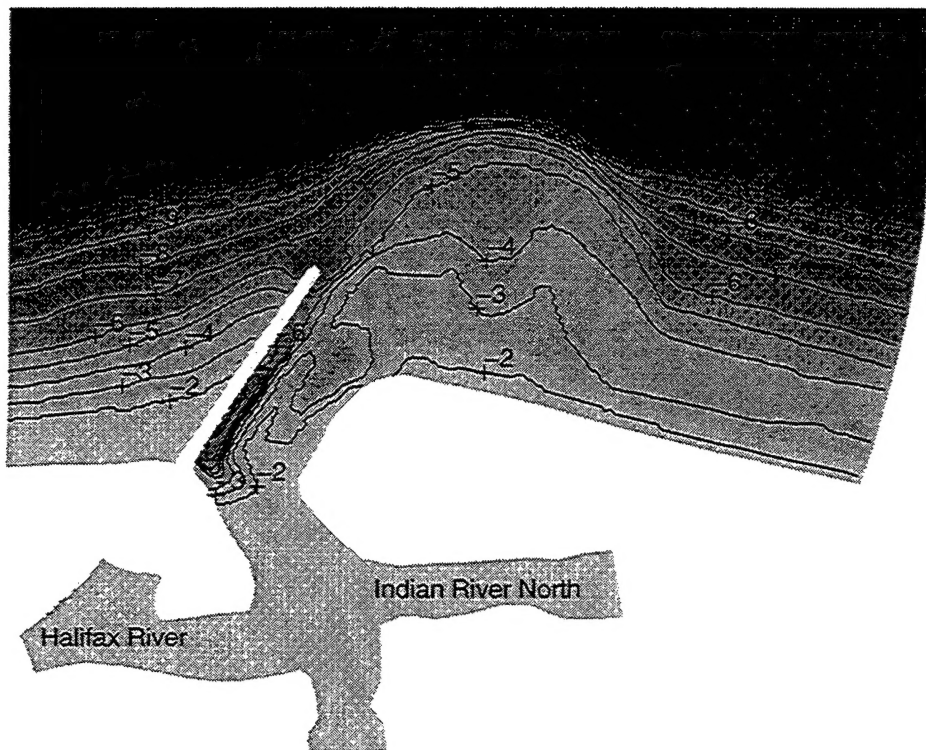
Figure 19: Bathymetry in Ponce de Leon Inlet (mean low water in meters)
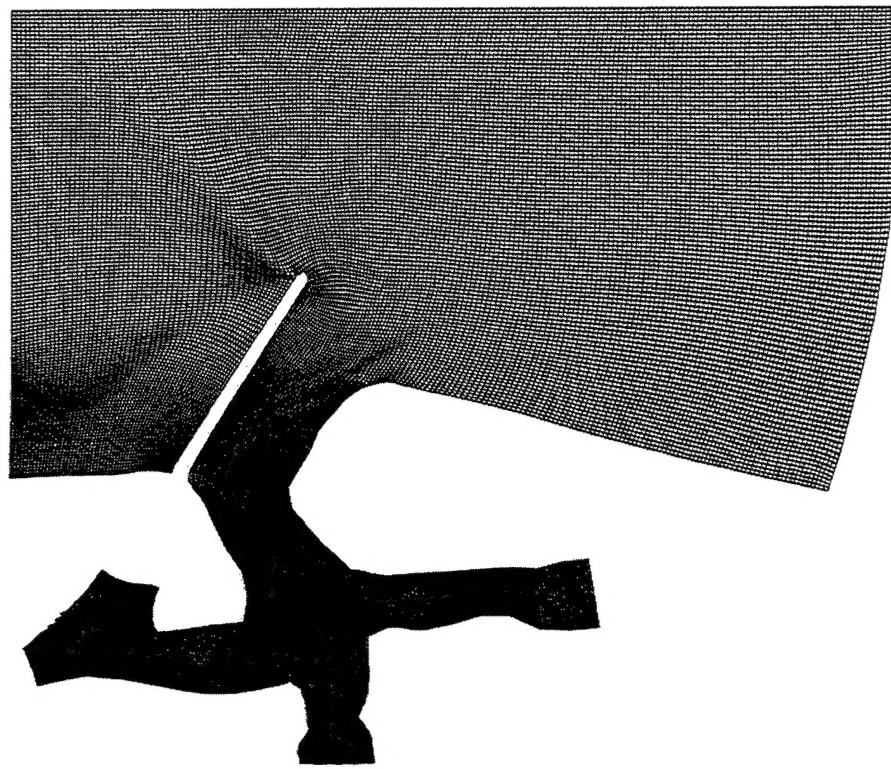
Figure 20: Computational grid in Ponce de Leon Inlet
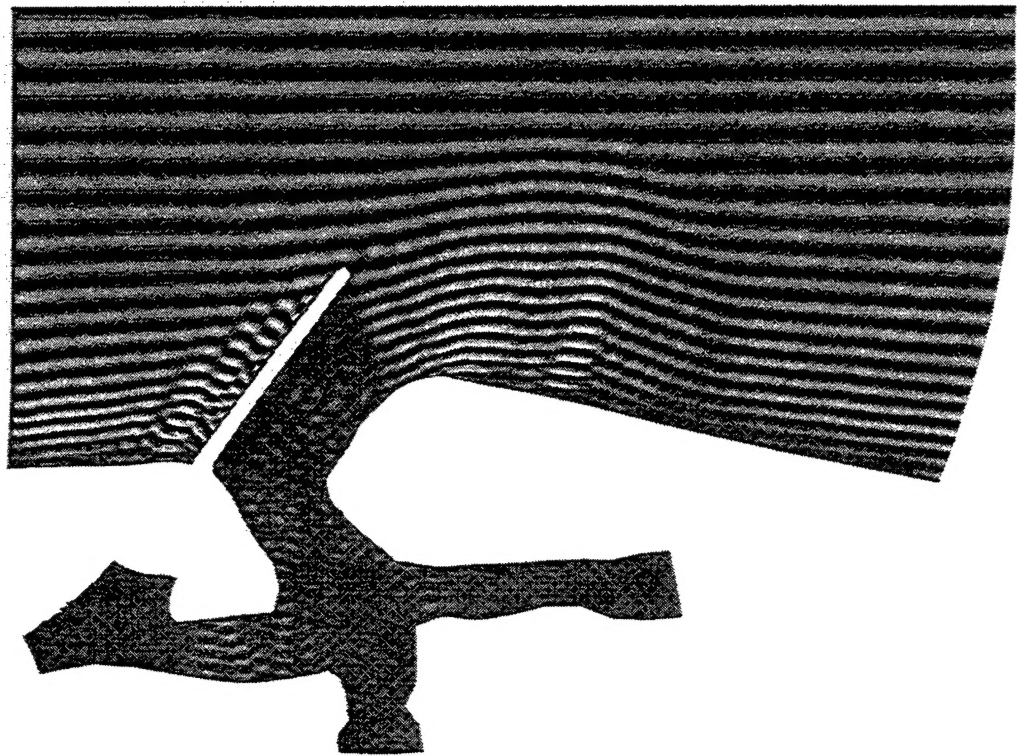
Figure 21: A snapshot of wave surface elevations in Ponce de Leon Inlet$(T = 15s)$